Mapping Spatial and Temporal Electrochemical Activity of Water and CO_2 Electrolysis on Gas-Diffusion Electrodes Using Infrared Thermography

Iglesias Van Montfort, Hugo Pieter; Burdyny, Thomas

DOI
10.1021/acsenergylett.2c00984

Publication date
2022

Document Version
Final published version

Published in
ACS Energy Letters

ACS Energy LETTERS

http://pubs.acs.org/journal/aelccp

Mapping Spatial and Temporal Electrochemical Activity of Water and CO_2 Electrolysis on Gas-Diffusion Electrodes Using Infrared Thermography

Hugo-Pieter Iglesias van Montfort and Thomas Burdyny*

Cite This: ACS Energy Lett. 2022, 7, 2410−2419

Read Online

ACCESS | Metrics & More | Article Recommendations | Supporting Information

ABSTRACT: Electrolysis of water, CO_2, and nitrogen-based compounds presents the opportunity of generating fossil-free fuels and feedstocks at an industrial scale. Such devices are complex in operation, and their performance metrics are usually reported as electrode-averaged quantities. In this work, we report the usage of infrared thermography to map the electrochemical activity of a gas-diffusion electrode performing water and CO_2 reduction. By associating the heat map to a characteristic catalytic activity, the presented system can capture electrochemical and physical phenomena as they occur in electrolyzers for large-scale energy applications. We demonstrate applications for catalyst screening, catalyst-degradation measurements, and spatial activity mapping for water and CO_2 electrolysis at current densities up to 0.2 A cm^{-2}. At these current densities we report catalyst temperature increases (>10 K for 0.2 A cm^{-2}) not apparent otherwise. Furthermore, substantial localized current density fluctuations are present. These observations challenge assumed local conditions, providing new fundamental and applied perspectives.

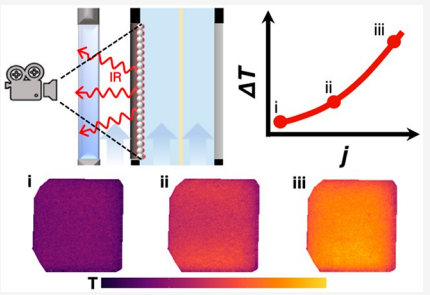

In the critical drive to find solutions for sustainable energy storage, electrochemical technologies which can be operated at global energy scales using fossil-free electricity offer promise. Research activities range broadly from the development of catalysts for novel reactions in nitrogen-based electrochemistry, steady improvement in C_2 and C_3 product selectivity for CO_2 reduction, to the fine-tuning of well-understood reactions such as water-splitting.[1−4] Performance metrics such as current density, efficiency/overpotential, selectivity, and stability provide the central foundation for evaluating electrochemical advancements and comparing systems.[5−7]

Despite electrochemical performance metrics being spatial and temporal properties (4D in space and time) which vary throughout a catalyst layer, these foundational metrics are measured as black box averaged quantities by potentiostats and bulk product quantification methods. All spatial information is then distilled to 1D resolutions in time. Not only are spatial resolutions in activity and selectivity lost, which results in phenomena and system behavior being indirectly evaluated, but electrochemistry is then faced with a one potentiostat−one data point problem. Catalyst screening efforts and mass data production for machine learning algorithms then subsequently suffer from insufficient or oversimplified data. Further, the dominant factors contributing to observed performance must be determined through multiple experiments and post-electrolysis analysis to properly disambiguate overlapping contributions of the catalyst, system, and operating parameters. With electrochemical behavior governed by phenomena spanning broad physical scales (angstroms to meters) and scientific domains, a more direct link between electrochemical activity and how we measure that activity is necessary.

Efforts toward the measurement of temporal−spatial electrochemical activity, as well as combinatorial setups, have been introduced to partially address these shortfalls, with an emphasis on catalyst activity.[8−14] However, most approaches still require the sequential testing of miniaturized reactors or cell segmentation, both of which have spatial resolutions set by physical limitations.[15−19] Multiwell dye-based techniques allow for parallelization but provide only indirect indicators of

Received: April 27, 2022
Accepted: June 28, 2022
Published: June 30, 2022

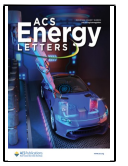

https://doi.org/10.1021/acsenergylett.2c00984
ACS Energy Lett. 2022, 7, 2410−2419

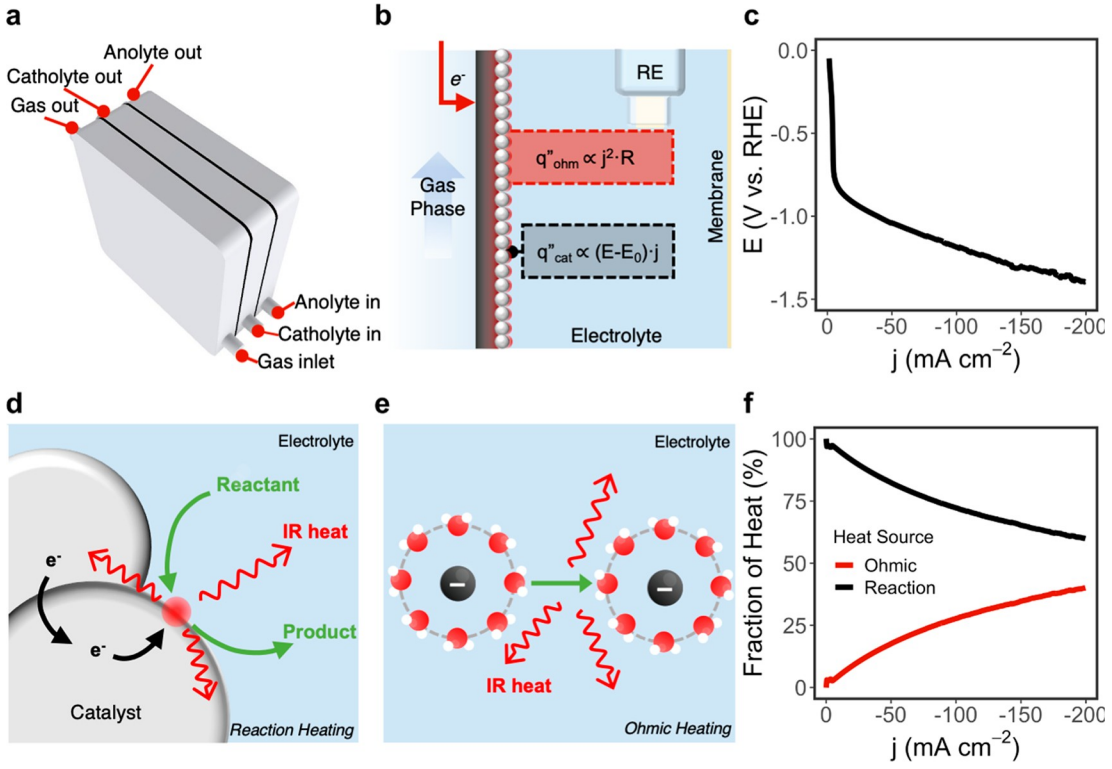

Figure 1. Heat production in a lab-scale electrolyzer is controlled mainly by catalytic and resistive overpotentials. (a) Schematic representation of a representative 3-compartment electrolyzer cell. (b) Half-cell view of an electrochemical cell using a catalyst deposited onto the liquid side of a gas-diffusion electrode. Heat generation locations and formula of ohmic heating (q''_{ohm}) and reaction-driven heating (q''_{cat}) are shown. (c) Polarization curve of a 100 nm Pt GDE during HER in the reported electrolyzer (1 M KOH catholyte, sweep rate of -1 mA cm^{-2} s^{-1}). (d) Heat is produced at the catalyst−electrolyte interface because of the overpotential required to drive the reaction. (e) Ohmic heating as a result of ion transport in an electrolyte. (f) Relative source of heating at the interface as a function of applied current density for a 15 mm thick 1 M KOH electrolyte.

electrochemical activity over a small catalyst, with tested current densities up to 50 mA cm^{-2}.[8,20] Dye techniques further rely on an observable liquid electrolyte resulting in cell configurations distanced from standard operation. Separately, thermographic approaches have been demonstrated in "quasi in situ" operation for fuel cell applications using membrane-electrode assemblies.[21−24] Here, an infrared camera observes the cathodic chamber where ambient oxygen may react with hydrogen that has crossed over from the anodic chamber. The exothermic reaction between hydrogen and oxygen then allows thermography to detect hydrogen crossover and subsequently pinholes in the ion exchange membrane and the effect of preparing membrane electrode assemblies. If an *operando* and accessible technique provided optical-level resolution of electrochemical activity under representative conditions, it would be not only valuable for catalyst testing but also broadly beneficial for both fundamental and applied analyses of the many rapidly advancing electrochemical fields.

In this study we exploit the typically undesired energy inefficiencies inherent in electrochemical reactions to observe location-specific catalytic activity via infrared thermography on gas-diffusion electrodes (GDEs) for water and CO_2 electrolysis applications. After testing the operating principles of the system, we proceed to display its functionality on a lab-scale electrolyzer (Figure 1A). We first demonstrate temperature deviations from ambient conditions as a function of applied current densities up to 0.2 A cm^{-2}, followed by a proof-of-concept set of experiments for spatial catalyst screening applications. The remainder of the work then highlights the substantial spatial and temporal variabilities in current density that exist during electrolysis on GDEs during water and CO_2 electrolysis, contradicting the assumed steady-state behavior.

In considering a means of directly probing localized reactions, we reflected that all electrochemical reactions are a result of charge transport. Subsequently, the current density (j) measured in our external circuits is the cumulative sum of all localized charge transport over an electrode's surface, and the voltage (V) represents the overpotentials needed to drive this transport. By nature, however, charge transfer and transport are fundamentally inefficient; a byproduct of inefficient transfer and transport is heat generation. It is important to note that the quantity of heat (q) produced at a catalyst's surface due to charge transfer scales linearly with current density ($q \propto j$), whereas heat produced by ohmic resistances in the electrolyte, for example, scale quadratically with the applied current density ($q \propto j^2$).[25] Thus, for an individual nanoparticle or region of an electrode, the local activity occurring should result in a proportional local heat generation. A characterization system capable of observing local heating can then in principle act as an indicator for electrochemical activity itself, opening the door for spatial and temporal mapping of catalytic activity with optical resolution.

As shown in Figure 1A,B, a commonly utilized GDE-based electrolyzer will generate heat in different cell locations during operation. We can estimate the quantity and location of heating that will occur in the cathodic chamber due to the catalyst heating (Figure 1D) and ohmic heating (Figure 1E) using known relations for heat generation (eqs S3 and S4). To

https://doi.org/10.1021/acsenergylett.2c00984
ACS Energy Lett. 2022, 7, 2410−2419

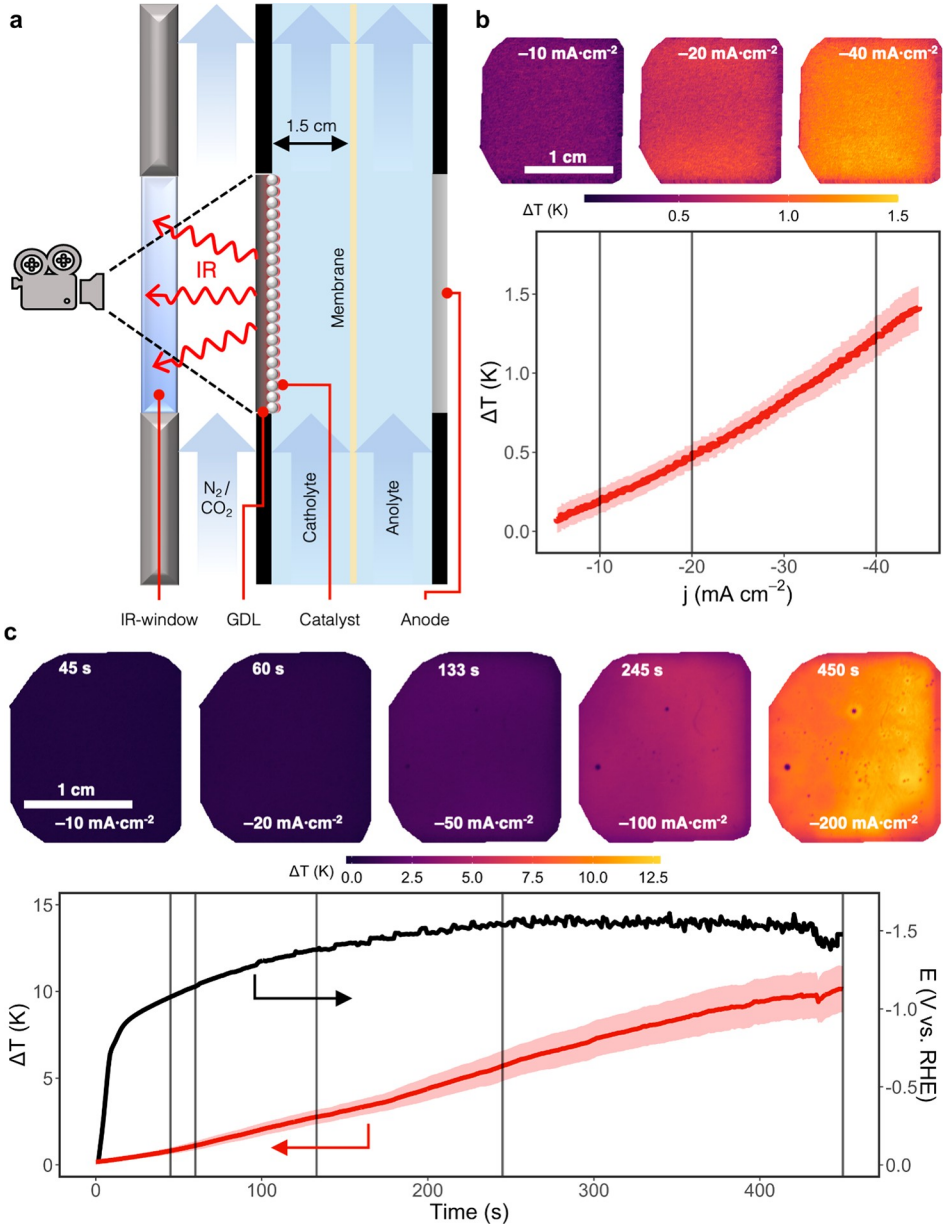

Figure 2. A windowed electrolyzer design allows sensing of catalytic activity on a gas-diffusion electrode (GDE). (a) Schematic depiction of the windowed electrolyzer and infrared (IR) imaging. (b) Thermographic stills of the back of the GDE with a 100 nm platinum catalyst layer and a stagnant electrolyte layer (1 M KOH). The observed catalyst area is 1.5 cm by 1.5 cm. (c) Average and standard deviation of temperatures across the back of the GDE during a 0 to −200 mA cm^{-2} polarization curve using a 100 nm silver catalyst layer and a 1 M KOH electrolyte flowing at 6 sccm. Vertical black lines indicate thermographic stills at various times and current densities of the polarization curve.

quantify this heat generation for a representative experiment, we performed a linear voltammetry scan (LSV) (Figure 1C) of hydrogen evolution on a platinum (Pt) electrocatalyst deposited onto a carbon GDE. Using the LSV data, the cell geometry, and eqs S3 and S4, we can predict the heat generated as a function of current density (Figures S1 and S2). As shown in Figure 1F, most of the heat generation for a 15 mm catholyte chamber occurs because of the overpotentials of the electrocatalyst at low current densities, with increasing contributions from ohmic heating at increased current densities. At 0.2 A cm^{-2}, overpotential and ohmic heating become similar. In cases where the catholyte chamber is only 1 mm, however, heat coming from the cathodic electrochemical reaction accounts for up to 95% of all heat generation (Figures S4 and S5).

From the above analysis we then posit that any temperature change of the catalyst, particularly at lower current densities, is primarily due to the heat generated from the electrochemical reactions on the cathode (e.g., $2H_2O + 2e^- \rightarrow H_2 + 2OH^-$). Observing the temperature changes of the catalyst during operation then acts as a measure of electrochemical activity, meaning that spatial and temporal variations in temperature can be linked to changes in the local quantity of reaction occurring. We then designed an experimental system capable of observing these temperature changes spatially and temporally and relating our observations to the reactions occurring on the catalyst.

https://doi.org/10.1021/acsenergylett.2c00984
ACS Energy Lett. 2022, 7, 2410−2419

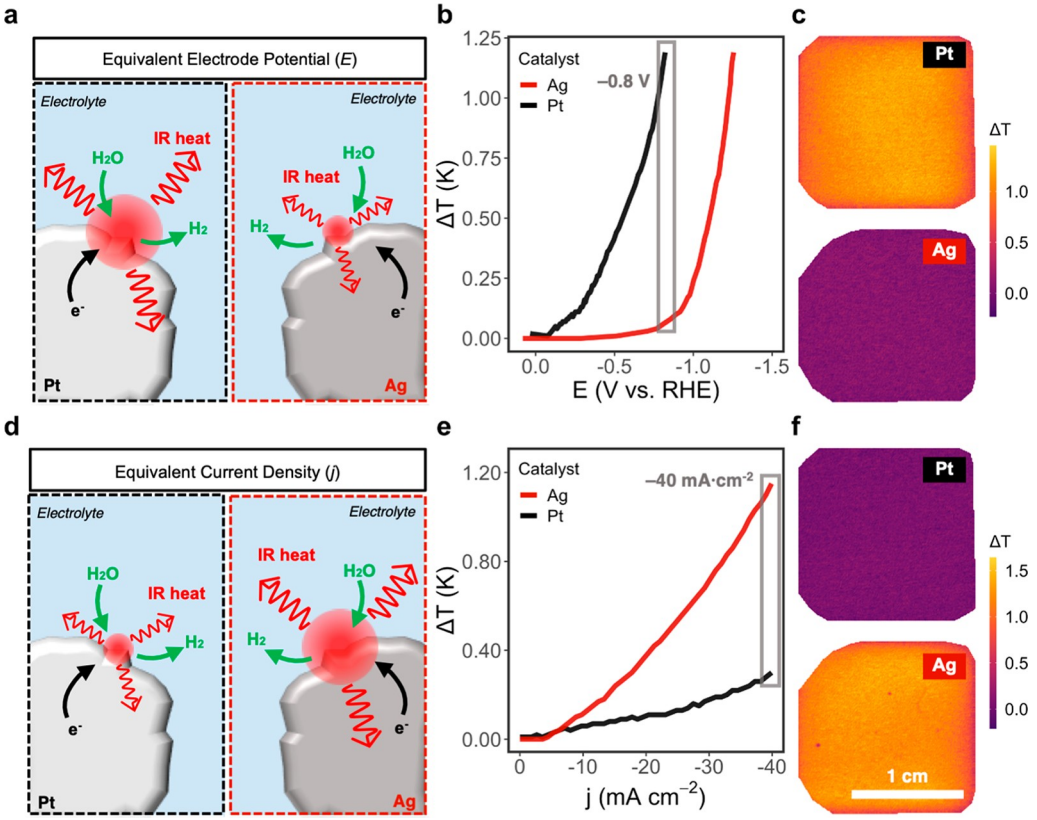

Figure 3. Electrode activity can be visualized using the spatial thermal-electric potentiostat. (a) At equal applied potentials, a more active catalyst will result in greater heat generation for the same reaction. (b) Combined thermal imaging and potentiostatic data showing a potential-dependence of the average temperature observed on Pt and Ag GDEs. The electrolyte is 1 M $KHCO_3$ flowing at 6 sccm. (c) Thermographic stills of the Pt and Ag GDEs at −0.8 V vs RHE. (d) At equal current density, a less active catalyst will result in greater heat generation for the same reaction. (e) Combined thermal imaging and potentiostatic data showing a current density dependence of the average temperature observed on Pt and Ag GDEs. The electrolyte is 1 M $KHCO_3$ flowing at 6 sccm. (f) Thermographic stills of the Pt and Ag GDEs at −40 mA cm^{-2}.

The calculations mentioned above indicated that catalyst temperature changes can be linked to the quantity of reactions occurring. Measuring the temperature of the catalyst with high spatial resolution in *operando* is practically challenging, however, because physical instrumentation is intrusive. Here we applied infrared thermography to record the temperature at the back of the GDE with spatial resolution (Figures 2A and S6−S9). The operation and configuration of the original electrochemical cell remains unaltered through the use of a gastight IR transparent window positioned in the gas channel, providing data representative of standard high-performance metrics works in applications such as CO_2 electrolysis.[1,26]

Notably, the temperature at the back of the GDE is not the same as the temperature of the catalyst embedded in the liquid electrolyte. However, through control experiments described here and calculations presented in the Supporting Information we have confirmed that the temperature at the back of the GDE is representative of the catalyst temperature (see Figure S3 and the Supplementary Notes in the Supporting Information).

During cell operation the temperatures recorded by the infrared camera are coupled to a potentiostat to display the dynamics of our electrolyzer in an *operando* mode. Shown in Figure 2B is an example case where we measured the GDE temperature of a sputtered 200 nm Pt electrode in 1 M KOH during a current density ramp rate of −0.45 mA cm^{-2} s^{-1}. Over a current density range of 0 to −40 mA cm^{-2}, relatively large temperature changes of ∼1.5 K are observed compared to the camera's sensitivity (<0.02 K). Further, chronopotentiometry tests performed with the Pt electrode at −20 and −200 mA cm^{-2} with elevated catholyte flow rates (20 sccm) show a rapid GDE temperature change within 10 s of operation (Figures S10−S12). The catholyte and anolyte temperatures, however, only gradually increase despite the high flow rates. These curves confirm that substantial heating occurs in the catalyst layer and that elevated temperatures are reached before heat production in the catalyst layer is balanced by heat dissipation from the gas and electrolyte convective flows. Importantly, upon the removal of an applied potential, the GDE temperature quickly decays back to that of the electrolyte temperature, providing an indication of the system's response time (Figure S13). The rapid decrease highlights the system's ability to measure both increasing and decreasing activity fluctuations during operation providing an avenue for spatial and temporal current density approximations. We can then confirm that infrared thermography can measure temperature changes, and thus electrochemical activity, at low reaction rates. Further, as calculated in the Supporting Information Supplementary Notes, we confirm that the GDE's heat conduction is dominant versus the electrolyte. These results act as a proof-of-concept that electrochemical activity, and its fluctuations in time, can be observed through infrared thermography.

https://doi.org/10.1021/acsenergylett.2c00984
ACS Energy Lett. 2022, 7, 2410−2419

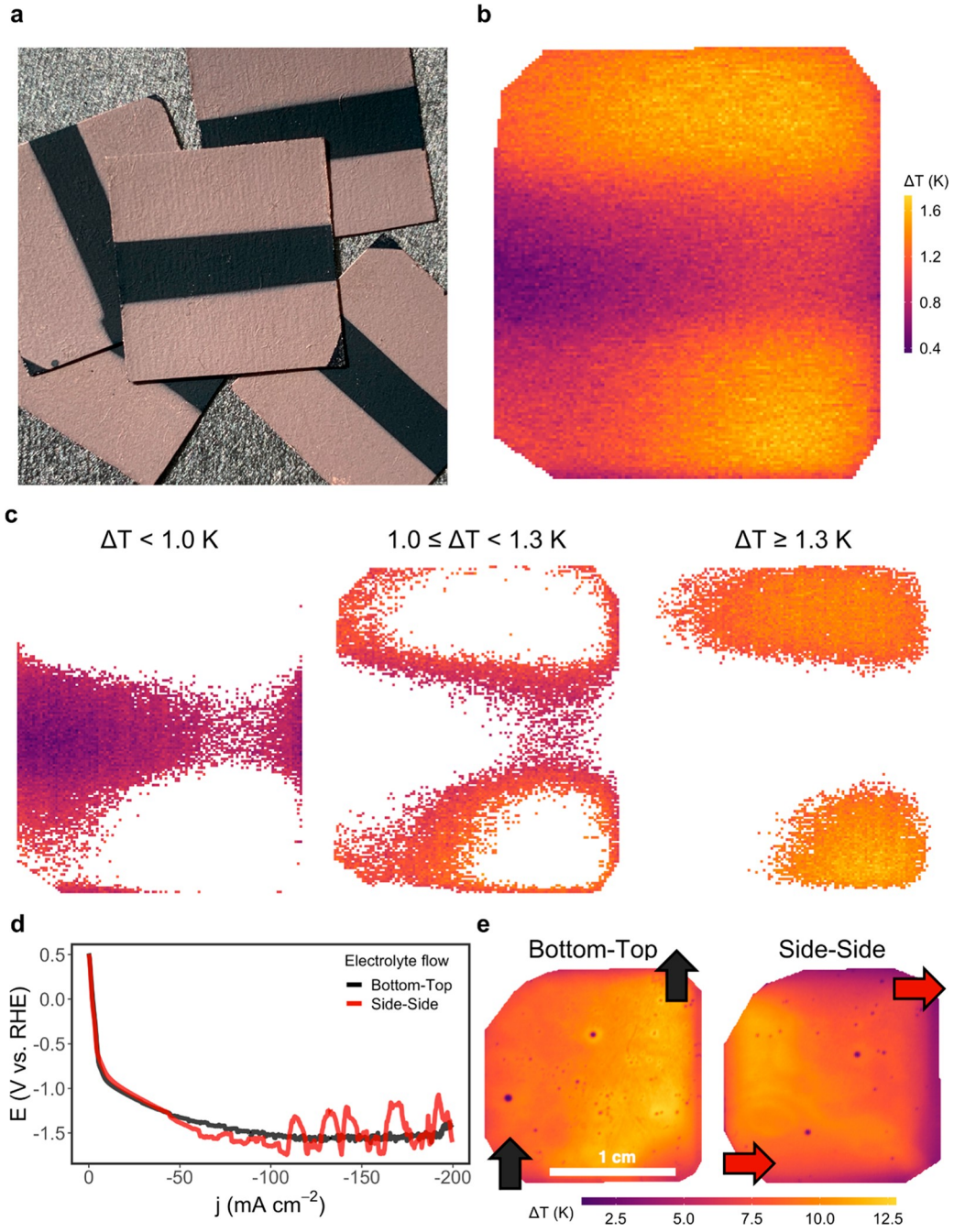

Figure 4. ***Operando*** **infrared thermography is effective for defect detection and sensing of current density distribution over an electrocatalyst's surface. (a) Gas-diffusion electrodes (GDE) with a surface copper layer and catalyst-free defects applied by masking during deposition. (b) Thermographic still of a defected copper GDE at −50 mA cm^{-2} with 1 M KOH flowing at 6 sccm. (c) Binned individual pixels of the still image in panel b as a function of temperature increase. (d) Polarization curves under the same electrolyte flow directions in panel e, where the influence of bubble accumulation is observed at voltage fluctuations. (e) Thermographic stills of a 100 nm Ag electrode with different electrolyte flow configurations at −200 mA cm^{-2}.**

We then turned to a 100 nm thick Ag sputtered catalyst deposited onto a GDE (see the Supporting Information for details) to demonstrate the spatial−temporal capabilities of our system under conditions known to cause failure via flooding of the GDE.[27] Here, N_2 gas is passed through the gas channel at the back of the GDE, and hydrogen evolution via water electrolysis takes place on the Ag catalyst. In Figure 2C the current density is ramped from 0 to −200 mA cm^{-2} at a rate of −0.45 mA cm^{-2} s^{-1}. Thermographic stills corresponding to timestamps of −10, −20, −50, −100, and −200 mA cm^{-2} highlight the rapid change in temperature as reaction rate increases, as well as the spatial effects occurring across the electrode. Near the end of the experiment, for example, perspiration of the electrolyte is observed. The lower temperatures of these droplets can be explained by evaporation of the water droplets by the nonhumidified N_2 stream. However, we note that the actual droplet temperatures are overestimated from those presented in Figure 2C because of the different emissivity of water (0.98) versus the corrected carbon emissivity (0.81).

https://doi.org/10.1021/acsenergylett.2c00984
ACS Energy Lett. 2022, 7, 2410−2419

A critical takeaway from the Ag linear sweep, however, is that by the end of the <8 min experiment the temperature of the nonwetted portions of the GDE had already increased by 10 K. Such a large temperature change influences the ongoing electrochemical reaction kinetics. For example, kinetic studies on a Pt electrode in 0.1 M KOH showed an exchange current density change of almost 2-fold for temperature changes from just 298 to 308 K.[28] In electrochemical systems with competing reactions, large temperature changes would then also impact the relative reaction rates, influencing Faradaic efficiencies. For fields such as CO_2 electrocatalysis, where current densities of >1 A cm^{-2} are reported for single- and multicarbon products, our findings indicate that 10−30 K catalyst temperature swings are not unfathomable depending on the system configuration. These demonstrations highlight just how quickly and by how much electrocatalyst temperatures are elevated during operation, which is critical for mass transport, thermodynamic, and kinetic models where temperatures are traditionally assumed as fixed quantities.

With the concept and response of the thermography system proven, we now provide a series of applications to demonstrate the capabilities of the technique for comparing catalysts, spatial activity mapping, and different electrochemical reactions.

Thus far we have focused on the link between heat and reaction rates. If our method can sense activity occurring in the catalyst layer, the overpotential of the reaction should also be discernible through temperature measurements. Specifically, we asked if the technique can be a useful means of measuring both the onset potential of a given catalyst and comparing the activities of different materials when coupling the thermal data from the IR camera and electric data from the potentiostat.

Using the previously described Pt and Ag catalyst layers on GDEs, we observed temperature changes with the camera system under increasing current densities of −0.45 mA cm^{-2} s^{-1} (Figure S14). As an established catalyst for hydrogen evolution, Pt should generate more heat than the poor HER Ag catalyst at a fixed electrode potential because of greater charge transfer (Figure 3A). These assumptions are confirmed by comparing the thermal signal against the electrode potential, where at a fixed potential of −0.8 V vs a reversible hydrogen electrode (RHE) the Pt catalyst has increased in temperature by 1 K, while the relatively inactive Ag catalyst shows minimal increases (Figure 3B,C). The combination of thermal-electric data further shows the vast difference in onset potential of the two catalysts, demonstrating a means to use ΔT versus overpotential for numerous catalysts on the same electrode. The reversed scenario where temperature evolution is instead compared at fixed reaction rates has the opposite effect (Figure 3D). Here, the more efficient Pt catalyst shows a lower temperature change than Ag at a comparable reaction rate (Figure 3E,F).

The catalyst comparisons between Ag and Pt in Figure 3 demonstrate the potential for screening catalysts in a combinatorial fashion on a singular GDE, using local temperature as an indicator of spatial reaction rate (Figure 3B) or overpotential (Figure 3E). Using our acquisition system, the temperature of individual groups of pixels can be analyzed during a reaction, allowing for temperature versus reaction rate or overpotential curves to be plotted for multiple catalysts on the same GDE at once. Such an approach can overcome the one potentiostat−one data point challenge for single-product reactions.

Beyond catalytic screening applications, spatial mapping of catalyst activity provides an additional means of examining key transport phenomena, limiting chemical reactions, and changes in behavior over time. In electrochemical systems, uneven current distributions across a catalyst will result from poor catalyst deposition, differently aging portions of the electrode, and spatially varying operating conditions (reactant concentrations, pressure, etc.), all of which are undesired. Defining a noninvasive probing mechanism to assess activity distribution is thus attractive for both laboratory and scale-up efforts. Here, we identify applications for spatial mapping, as well as fundamental resolution limitations of the approach.

To simulate a catalyst region which may have been removed or deactivated during operation, we partially masked a portion of a GDE's microporous layer (MPL) prior to depositing a 100 nm thick copper (Cu) catalyst (Figure 4A). After a linear current density ramp to −50 mA cm^{-2}, the current density was kept constant. Here, distinctive heating patterns corresponding to the catalyst layer formed as a result of the electrochemical reactions occurring (Figure 4B). The upper and lower hotter bands correspond to the coated sections of the GDE, while the cooler central region is the bare carbon MPL which has lower HER activity.[27] It can then be deduced that the static −50 mA cm^{-2} applied to the system (112.5 mA total) is not equally distributed over the electrode, with the Cu regions experiencing reaction rates much higher than the average value imposed by the potentiostat.

The probing technique further allows for individual analysis per pixel, which means an image can be binned based on the individual value of each dot and tracked over time. Binning the readings results in a clearer picture (Figure 4C), where we can see the central part of the GDE reading considerably lower temperatures than the other two bins. In this experiment, the temperature distribution effects linked to the electrolyte flow patterns in the system can also be observed. Higher overall temperatures are binned at the exit side of the reactor (top-right) and in the stagnant electrolyte regions (bottom-right and top-left).

The spatial and temporal resolution of the presented technique is mainly influenced by two distinct factors. On one hand, the (an)isotropy of the electrode support material: for anisotropic carbon GDEs with better in-plane heat conduction than through-plane conduction, the resolution can be expected to be affected more heavily by the thickness of the electrode. This is because heating occurs within the catalyst layer, while temperature is detected at the back of the GDE. Temperature dispersion will then occur, which is a reason why the catalyst−defect interface in Figure 4b is not more distinct. Second, excessive heat retention or evacuation by the device also influences temporal resolution. As heat transfer is dependent upon the magnitude of temperature differences, smaller or larger temperature changes will impact heat transfer and system response time. Thus, a small temperature difference would result in a longer cooling time, whereas a high temperature difference would decrease this.

Following from the observations of the defected catalyst layer, we wanted to better understand how the catholyte and anolyte can influence the reaction rate distribution across a catalyst layer. To this end we varied the flow direction of the anolyte and catholyte flow from a bottom-to-top direction to a side-to-side direction. While in the cathode chamber product gases diffuse into the gas channel prior to nucleating, the anodic reaction performed here is the oxygen evolution

https://doi.org/10.1021/acsenergylett.2c00984
ACS Energy Lett. 2022, 7, 2410−2419

reaction (OER) which results in substantial generation of O_2 bubbles. In the side-to-side configuration, gas bubbles become trapped in the anode compartment, resulting in a noticeably less stable linear sweep voltammetry measurement (Figure 4D). Such disturbances in the anode compartment are further shown to cause rapidly changing temperature profiles of the cathode GDE. During operation, cloud-like heating patterns are observed to move across the cathode even though no bubbles are present in the catholyte (Figures 4E and S15), which is not observed during bottom-to-top flow. These variations are best viewed in Movies 1 and 2 in the Supporting Information.

As no gas evolution is present in the cathode chamber, we suspect that the buildup of gas in the anode chamber is partially shielding the nickel mesh anode. Any portion of the anode that is shielded will then impact the anodic current density distribution, and we suspect that the temperature variations observed on the cathode are a result of this uneven current density distribution. Such increases and decreases in activity would not only result in faster catalyst aging but also indicate that the voltage and current density of an electrocatalyst are highly variable.

The collective spatial observations presented in this section point to many experimental systems having a less homogeneous reaction environment than indicated through purely potentiostatic data. These considerations are particularly important within elevated current density experiments where large reaction rate changes occur with minimal changes in overpotential, implying a higher variance across the electrode's surface.

A known unwanted side-reaction in CO_2 electrolyzers is the reaction of reactant CO_2 with byproduct hydroxide, which lowers device utilization and represents one of the technology's largest practical barriers.[7,29,30] The parasitic reaction which forms carbonates and precipitates is highly exothermic in nature and occurs within the liquid-immersed catalyst layer (Figure 5A). The generated heat then should be discernible with our camera.

Using a Ag catalyst that is adept at CO_2 conversion to CO, we compared the thermal-electric data of the catalyst in both a CO_2 and an N_2 environment. A CO_2 feed will produce primarily CO, while an N_2 feed only produced H_2. Considering first the electrical data, a lower overpotential is shown for the CO_2 gas-flow, which can be explained by Ag being a better CO_2 reduction catalyst than HER catalyst (Figure 5B). When observing the thermal data (Figure 5C), however, 1−2 K greater temperatures are observed in the CO_2 gas flow case. As CO_2 reduction to CO and HER have similar thermoneutral half-cell potentials (see Tables S1 and S2 in the Supporting Information), these temperature changes are ascribed to the exothermic interaction between CO_2 and hydroxide.

Importantly, a control experiment where the gaseous CO_2 feed was stopped at 0 mA cm^{-2} showed a temperature decrease of only around 0.2 K (Figure S16). Such a result is reasonable as the absolute moles of neutralized hydroxide in a stagnant electrolyte film is substantially lower than is generated at −200 mA cm^{-2}.

Another interesting observation can be made from the electrode's average temperature (Figure 5C) after 60 s. Here the electrode's temperature rapidly increased to values ∼10 K above room temperature. Much like in the HER case above, these increased surface temperatures have implications for mass transport and density functional theory models which

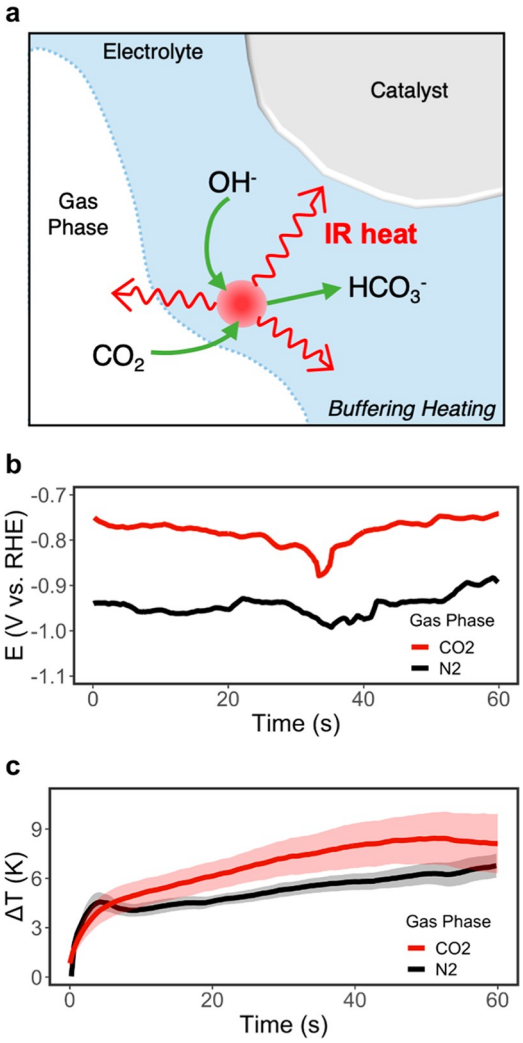

Figure 5. The heat effects of CO_2 dissolution are comparable to reaction-driven heating at elevated current densities. (a) CO_2 dissolves in alkaline media to form (bi)carbonates in an exothermic reaction. (b) Reaction potentials under an N_2 and CO_2 gas flow at a 100 nm Ag GDE using 1 M KOH at a fixed current density of −200 mA cm^{-2}. Under N_2 the primary reaction is hydrogen evolution. Under CO_2 gas flow the primary reaction is CO_2 reduction. (c) Temperature increases over the GDE surface for the sequences in panel b, where the CO_2 reduction case displays a noticeably higher overall temperature despite lower applied potentials.

presently do not consider activity−temperature relationships.[31−33] For example, the solubility of CO_2 in water decreases by ∼30% from 298 to 308 K, while solubility limits for salts will increase.

Besides the average temperature of the electrode, it is also worth noting the deviation in observed temperature changes. The electrode performing CO2RR displayed, under the same conditions, a much wider temperature distribution than the one performing HER. This could be blamed on entrance effects of the gas feed resulting in increased CO_2 dissolution in the entrance region of the GDE. However, seeing as the feed of CO_2 (20 sccm) is considerably higher than its consumption in the electrocatalytic process (at 200 mA cm^{-2}, 2 orders of magnitude difference), it is safe to assume that the increased variance in temperatures is an indicator of at least some degree of poorer current-density distribution upon performing

https://doi.org/10.1021/acsenergylett.2c00984
ACS Energy Lett. 2022, 7, 2410−2419

CO2RR on these electrodes. This highlights the blind spot in CO2RR literature when it comes to spatial distribution effects on catalytic performance of showcased electrolyzer solutions.

For the complex catalytic pathways observed in CO_2 reduction, heat effects are also of noticeable influence on the selectivity of the catalyst. For example, copper electrodes have been shown to vary selectivity with changes in temperature.[34−36] Additionally, improved mass transfer of reactants can be expected at hot spots, as viscosity of water and diffusion of gases in the interface are affected by temperature.[37,38] For scale-up purposes, maintaining the similarity of electrochemical activity across a surface is necessary to ensure understanding of the behavior of the system.[39,40] The ability of thermography to indirectly scope activity over a surface during operation presents a chance to gain more information from experiments, aiding in catalyst and system advances.

The concept of utilizing infrared emissions as a direct indicator of catalytic activity provides a broad set of potential applications for the ever-growing set of novel electrochemical reactions under investigation. The high emissivity of common carbon provides an *operando* time and location-specific measure of activity at backbonesoptical resolutions, which can be coupled with electrical data analysis. Through a series of demonstrative applications, we show the propensity for infrared thermography to link measured changes in the gas-diffusion layer temperature to reaction overpotentials, catalyst type, defect sites on the catalyst layer, and dissolution of CO_2 into the electrolyte during CO_2 electrolysis. The substantial catalytic temperatures observed during regular operation highlight the need to reinterpret assumed kinetic data and reaction environments for these important electrochemical reactions.

METHODS AND MATERIALS

Methods. *Infrared Imaging.* The camera system used consisted of an FLIR SC7650 with a 25 mm fixed-focal length objective and an f/2.5 aperture. The manufacturer's software, AltaIR, was used to control the camera and preprocess the acquired data. All images we include in the report are taken at a quarter-size resolution (320 × 256 pixels of the maximum 640 × 512 possible), at a refresh rate of 25 Hz and subsampling of 1/10 frames. This means, ultimately, that the acquisition frequency of the system is 2.5 fps. This allowed us to keep the footage from exceeding 1 GB per file. Temperature resolution depends on two factors: the sensitivity of the camera and the calibration. The manufacturer states noise-levels of as low as 20 mK, while the camera we used was calibrated for a range of 16−85 °C.

We performed all experiments in an enclosed box (a repurposed Faraday-cage, Figure S7) to avoid any reflections from the lab in interfering in the measurements. The end plate of the electrolyzer was covered using scotch tape to ensure no reflections from the metallic surface would interfere with the irradiation of the GDE.

The camera records thermal images at spectral wavelengths between 3.0 and 5.0 μm. At these wavelength, the transmittance values of the sapphire window were approximated to be 90%. In order to translate the recorded emittance from the GDE backbone to a true temperature value, we compared the irradiation at room temperature of the GDE through the window and a piece of carbon tape with emissivity values of 0.8−0.9, which we approximated as 0.85.[40,41] The results from this calibration measurement are displayed in Figure S8. The value of the corrected GDE emissivity of 0.81 coincides with the irradiation reading of the carbon tape, whereas the uncorrected GDE irradiation value is above the latter. These measurements were performed by comparing an identical number of pixels of the GDE and the carbon tape, as can be seen in Figure S9.

Electrochemical Testing. Electrolyte was pumped through the anolyte and catholyte chambers using a peristaltic pump, with a minimum rate of 6 sccm. The gas-phase stream used was either N_2 (for all water-splitting runs) or CO_2 (for all CO2RR runs), which we controlled using a mass-flow controller (MFC, Bronkhorst EL-FLOW Select). The pressures of the gas and liquid channels were controlled using three back-pressure regulators (BPR), one after each flow channel. A mass-flow meter (MFM) was connected to the effluent gas stream which subsequently flowed to a liquid trap and then an in-line gas chromatograph (GC). The full instrumentation and flow setup is sketched in Figure S6.

Electrochemical experiments were performed using a Versastat MC-1000 potentiostat. All potentials reported are corrected for ohmic drops (85% correction applied) with resistances measured by electrochemical impedance spectroscopy (EIS) in a frequency range of 12550 to 1.5 Hz at OCV and the maximum current applied. These routines were performed in sync with the camera system, to obtain thermographs that could be coupled to the time stamps of the potentiostat readings. Experiments were performed in both stepped current mode and chronopotentiometry as detailed for the experiments in the main text.

Materials. For all tests detailed in this study we used a modular electrolyzer, based on three separate flow chambers of PTFE with spacing gaskets in between. Metal end plates were added to ensure even cell compression. To enable IR filming of the gas diffusion electrode (GDE), the PTFE gas compartment was fully cut through and a sapphire window was integrated in the design in place of the PTFE wall (see Figures 2a and S7). The device was tested for leaking during operation using a mass-flow controller on the gas-inlet stream and a mass-flow meter on the gas-outlet stream to ensure the mass flow in was equivalent to the mass flow out. The catholyte used was either 1 M KOH (Sigma-Aldrich 99.99% semiconductor grade) or 1 M $KHCO_3$ (Sigma-Aldrich 99.7% ACS reagent). The anolyte was always 1 M KOH to reduce total cell potential. The catholyte and anolyte compartments in the electrolyzer were separated by a Nafion-115 cation-exchange membrane.

Freudenberg H14C10 gas-diffusion layers were used as GDEs in all experiments with a manufacturer-reported thickness of 175 μm (δ_{gde} = 175 μm). Catalyst layers of a nominal thickness of 100 nm were deposited using DC magnetron sputtering at a pressure of 3 μbar. Introduction of defects on these layers was achieved by shielding a region of the hydrophobic microporous layer with titanium masks during deposition.

The infrared imaging camera (FLIR SC7650) was equipped with a fixed focal length concave lens of 25 mm (FLIR) and controlled using ALTAIR software. The window in the PTFE cell was an Edmund Optics uncoated sapphire (δ = 1 mm and ⌀ = 23.75 mm). All measurements were performed in a dark box (see Figure S7) to avoid infrared contamination by external sources and unwanted reflections.

https://doi.org/10.1021/acsenergylett.2c00984
ACS Energy Lett. 2022, 7, 2410−2419

■ ASSOCIATED CONTENT

Supporting Information

The Supporting Information is available free of charge at https://pubs.acs.org/doi/10.1021/acsenergylett.2c00984.

Reasoning on the working criteria for the thermography system and source of heat-sensed Supplementary References (1−5) Figures S1 to S15 Supporting figures, experimental setup and response time of the system (PDF)

Movie S1: Recording of polarization of a Ag gas-diffusion electrode performing hydrogen-evolution in a side-side electrolyte flow configuration (MP4)

Movie S2: Recording of polarization of a Ag gas-diffusion electrode performing hydrogen-evolution in a bottom-top electrolyte flow configuration (MP4)

■ AUTHOR INFORMATION

Corresponding Author

Thomas Burdyny − *Materials for Energy Conversion and Storage (MECS), Department of Chemical Engineering, Faculty of Applied Sciences, Delft University of Technology, 2629 HZ Delft, The Netherlands;* orcid.org/0000-0001-8057-9558; Email: t.e.burdyny@tudelft.nl

Author

Hugo-Pieter Iglesias van Montfort − *Materials for Energy Conversion and Storage (MECS), Department of Chemical Engineering, Faculty of Applied Sciences, Delft University of Technology, 2629 HZ Delft, The Netherlands;* orcid.org/0000-0002-9594-392X

Complete contact information is available at: https://pubs.acs.org/10.1021/acsenergylett.2c00984

Author Contributions

Conceptualization: H.-P.I.v.M. and T.B. Methodology: H.-P.I.v.M. Investigation: H.-P.I.v.M. and T.B. Visualization: H.-P.I.v.M. and T.B. Funding acquisition: T.B. Project administration: H.-P.I.v.M. Supervision: T.B. Writing−original draft: H.-P.I.v.M. Writing−review and editing: H.-P.I.v.M. and T.B.

Funding

H.-P.I.v.M. and T.B. acknowledge the cofinancing provided by Shell and PPP-allowance from Top Consortia for Knowledge and Innovation (TKI's) of the Ministry of Economic Affairs and Climate in the context of the e-Refinery Institute.

Notes

The authors declare the following competing financial interest(s): H.-P.I.v.M. and T.B. of the Delft University of Technology have filed provisional patent application no. 2028898 regarding the method and configuration for observing catalytic activity via infrared radiation.

All data represented are available in a condensed form. Infrared recordings are available in both the IR camera's proprietary file type and exported mp4 files.

■ ACKNOWLEDGMENTS

The authors acknowledge Joost Middelkoop for assistance with setting up the experimental systems for product detection, Herman Schreuders for mentioning we "had an old IR-camera" lying around and sparking the idea for this project, and Dr. Erdem Irtem for suggesting ways to improve bubble evacuation from the electrolyzer.

■ REFERENCES

(1) García de Arquer, F. P.; et al. CO_2 electrolysis to multicarbon products at activities greater than 1 A cm^{-2}. *Science* **2020**, *367*, 661−666.

(2) Kim, T.; Palmore, G. T. R. A scalable method for preparing Cu electrocatalysts that convert CO_2 into C_{2+} products. *Nat. Commun.* **2020**, *11*, 3622.

(3) Chen, G. F.; et al. Electrochemical reduction of nitrate to ammonia via direct eight-electron transfer using a copper−molecular solid catalyst. *Nat. Energy* **2020**, *5*, 605−613.

(4) Wu, Z. Y.; et al. Electrochemical ammonia synthesis via nitrate reduction on Fe single atom catalyst. *Nat. Commun.* **2021**, *12*, 2870.

(5) Nwabara, U. O.; Cofell, E. R.; Verma, S.; Negro, E.; Kenis, P. J. A. Durable Cathodes and Electrolyzers for the Efficient Aqueous Electrochemical Reduction of CO_2. *ChemSusChem* **2020**, *13*, 855.

(6) Chan, K. A few basic concepts in electrochemical carbon dioxide reduction. *Nat. Commun.* **2020**, *11*, 5954.

(7) Rabinowitz, J. A.; Kanan, M. W. The future of low-temperature carbon dioxide electrolysis depends on solving one basic problem. *Nat. Commun.* **2020**, *11*, 5231.

(8) Reddington, E.; et al. Combinatorial electrochemistry: A highly parallel, optical screening method for discovery of better electrocatalysts. *Science* **1998**, *280*, 1735−1737.

(9) Fernández, J. L.; Raghuveer, V.; Manthiram, A.; Bard, A. J. Pd-Ti and Pd-Co-Au electrocatalysts as a replacement for platinum for oxygen reduction in proton exchange membrane fuel cells. *J. Am. Chem. Soc.* **2005**, *127*, 13100−13101.

(10) Gerken, J. B.; Shaner, S. E.; Massé, R. C.; Porubsky, N. J.; Stahl, S. S. A survey of diverse earth abundant oxygen evolution electrocatalysts showing enhanced activity from Ni-Fe oxides containing a third metal. *Energy Environ. Sci.* **2014**, *7*, 2376−2382.

(11) Ye, H.; Park, H. S.; Bard, A. J. Screening of electrocatalysts for photoelectrochemical water oxidation on W-doped BiVO4 photocatalysts by scanning electrochemical microscopy. *J. Phys. Chem. C* **2011**, *115*, 12464−12470.

(12) Guevarra, D.; et al. Development of solar fuels photoanodes through combinatorial integration of Ni-La-Co-Ce oxide catalysts on BiVO4. *Energy Environ. Sci.* **2016**, *9*, 565−580.

(13) Fosdick, S. E.; Berglund, S. P.; Mullins, C. B.; Crooks, R. M. Evaluating electrocatalysts for the hydrogen evolution reaction using bipolar electrode arrays: Bi- and trimetallic combinations of Co, Fe, Ni, Mo, and W. *ACS Catal.* **2014**, *4*, 1332−1339.

(14) Kim, D. K.; Maier, W. F. Combinatorial discovery of new autoreduction catalysts for the CO 2 reforming of methane. *J. Catal.* **2006**, *238*, 142−152.

(15) Ghosh, P. C.; et al. In situ approach for current distribution measurement in fuel cells. *J. Power Sources* **2006**, *154*, 184−191.

(16) Reshetenko, T. V.; Bender, G.; Bethune, K.; Rocheleau, R. A segmented cell approach for studying the effects of serpentine flow field parameters on PEMFC current distribution. *Electrochim. Acta* **2013**, *88*, 571−579.

(17) Osmieri, L.; Mauger, S.; Ulsh, M.; Neyerlin, K. C.; Bender, G. Use of a segmented cell for the combinatorial development of platinum group metal-free electrodes for polymer electrolyte fuel cells. *J. Power Sources* **2020**, *452*, 227289.

(18) Lin, R.; Sander, H.; Gülzow, E.; Friedrich, A. Investigation of Locally Resolved Current Density Distribution of Segmented PEM Fuel Cells to Detect Malfunctions. *ECS Trans.* **2010**, *26*, 229−236.

(19) Gregoire, J. M.; et al. Improved fuel cell oxidation catalysis in Pt1-X TaX. *Chem. Mater.* **2010**, *22*, 1080−1087.

(20) Hitt, J. L. A high throughput optical method for studying compositional effects in electrocatalysts for CO_2 reduction. *Nat. Commun.* **2021**, *12*, 1114 DOI: 10.1038/s41467-021-21342-w.

(21) Phillips, A.; Ulsh, M.; Neyerlin, K. C.; Porter, J.; Bender, G. Impacts of electrode coating irregularities on polymer electrolyte membrane fuel cell lifetime using quasi in-situ infrared thermography and accelerated stress testing. *Int. J. Hydrogen Energy* **2018**, *43*, 6390−6399.

(22) Wang, M.; et al. Visualization, understanding, and mitigation of process-induced-membrane irregularities in gas diffusion electrode-based polymer electrolyte membrane fuel cells. *Int. J. Hydrogen Energy* **2021**, *46*, 14699−14712.
(23) Das, P. K.; et al. Rapid detection of defects in fuel-cell electrodes using infrared reactive-flow-through technique. *J. Power Sources* **2014**, *261*, 401−411.
(24) Aieta, N. V.; et al. Applying infrared thermography as a quality-control tool for the rapid detection of polymer-electrolyte-membrane-fuel-cell catalyst-layer-thickness variations. *J. Power Sources* **2012**, *211*, 4−11.
(25) Catherino, H. A. Estimation of the heat generation rates in electrochemical cells. *J. Power Sources* **2013**, *239*, 505−512.
(26) Dinh, C. T.; et al. CO_2 electroreduction to ethylene via hydroxide-mediated copper catalysis at an abrupt interface. *Science* **2018**, *360*, 783−787.
(27) Yang, K.; Kas, R.; Smith, W. A.; Burdyny, T. Role of the Carbon-Based Gas Diffusion Layer on Flooding in a Gas Diffusion Electrode Cell for Electrochemical CO_2 Reduction. *ACS Energy Lett.* **2021**, *6*, 33−40.
(28) Tang, D.; Lu, J.; Zhuang, L.; Liu, P. Calculations of the exchange current density for hydrogen electrode reactions: A short review and a new equation. *J. Electroanal. Chem.* **2010**, *644*, 144−149.
(29) Huang, J. E.; et al. CO 2 electrolysis to multicarbon products in strong acid. *Science* **2021**, *372*, 1074−1078.
(30) Ozden, A.; et al. Cascade CO_2 electroreduction enables efficient carbonate-free production of ethylene. *Joule* **2021**, *5*, 706−719.
(31) Bohra, D.; Chaudhry, J. H.; Burdyny, T.; Pidko, E. A.; Smith, W. A. Modeling the electrical double layer to understand the reaction environment in a CO_2 electrocatalytic system. *Energy Environ. Sci.* **2019**, *12*, 3380−3389.
(32) Nesbitt, N. T.; et al. Liquid-Solid Boundaries Dominate Activity of CO_2 Reduction on Gas-Diffusion Electrodes. *ACS Catal.* **2020**, *10*, 14093−14106.
(33) Kas, R.; et al. Along the Channel Gradients Impact on the Spatioactivity of Gas Diffusion Electrodes at High Conversions during CO_2 Electroreduction. *ACS Sustain. Chem. Eng.* **2021**, *9*, 1286−1296.
(34) Ahn, S. T.; Abu-Baker, I.; Palmore, G. T. R. Electroreduction of CO_2 on polycrystalline copper: Effect of temperature on product selectivity. *Catal. Today* **2017**, *288*, 24−29.
(35) Hori, Y.; Kikuchi, K.; Murata, A.; Suzuki, S. Production of methane and ethylene in electrochemical reduction of carbon dioxide at copper electrode in aqueous hydrogencarbonate solution. *Chem. Lett.* **1986**, *15*, 897−898.
(36) Yang, B.; et al. Accelerating CO_2 Electroreduction to Multicarbon Products via Synergistic Electric-Thermal Field on Copper Nanoneedles. *J. Am. Chem. Soc.* **2022**, *144*, 3039−3049.
(37) Fuller, E. N.; Schettler, P. D.; Giddings, J. C. A new method for prediction of binary gas-phase diffusion coefficients. *Indsutrial Eng. Chem.* **1966**, *58*, 18−27.
(38) Kestin, J.; Sokolov, M.; Wakeham, W. A. Viscosity of liquid water in the range −8°C to 150°C. *J. Phys. Chem. Ref. Data* **1978**, *7*, 941−948.
(39) Prentice, G. *Electrochemical engineering principles*; Prentice Hall: New Jersey, 1990.
(40) Goodridge, F.; Scott, K. *Electrochemical process engineering: A guide to the design of electrolytic plant. Electrochemical Process Engineering*; Plenum Press, 1995. DOI: 10.1007/978-1-4899-0224-5.
(41) Fluke Process Instruments. Emissivity Values for Non-Metals | Fluke Process Instruments. *Fluke Process Instruments* https://www.flukeprocessinstruments.com/en-us/about-us/emissivity-values-non-metals (2019) (accessed 2020-05-07).

https://doi.org/10.1021/acsenergylett.2c00984
ACS Energy Lett. 2022, 7, 2410−2419